

Review

Magnetic Nanohydrometallurgy Applied to Lanthanide Separation

Fernando M. de Melo , Sabrina N. Almeida and Henrique E. Toma *

Instituto de Química, Universidade de São Paulo, São Paulo 05508-000, Brazil;
fernando.menegatti.melo@usp.br (F.M.d.M.); sabrina_nobrega@hotmail.com (S.N.A.)

* Correspondence: henetoma@iq.usp.br

Received: 24 April 2020; Accepted: 8 June 2020; Published: 11 June 2020



Abstract: Lanthanides play an important role in modern technology because of their outstanding optical, electronic, and magnetic properties. Their current hydrometallurgical processing involves lixiviation, leading to concentrates of elements whose separation requires exhaustive procedures because of their similar chemical properties. In this sense, a new nanotechnological approach is here discussed, involving the use of iron oxide nanoparticles functionalized with complexing agents, such as diethylenetriaminepentaacetic acid (DTPA), for carrying out the magnetic extraction and separation of the lanthanide ions in aqueous solution. This strategy, also known as magnetic nanohydrometallurgy (MNHM), was first introduced in 2011 for dealing with transition metal recovery in the laboratory, and has been recently extended to the lanthanide series. This technology is based on lanthanide complexation and depends on the chemical equilibrium involved. It has been better described in terms of Langmuir isotherms, considering a uniform distribution of the metal ions over the nanoparticles surface, as evidenced by high angle annular dark field microscopy. The observed affinity parameters correlate with the lanthanide ion contraction series, and the process dynamics have been studied by monitoring the nanoparticles migration under an applied magnetic field (magnetophoresis). The elements can be reversibly captured and released from the magnetically confined nanoparticles, allowing their separation by a simple acid-base treatment. It can operate in a circular scheme, facilitated by the easy magnetic recovery of the extracting agents, without using organic solvents and ionic exchange columns. MNHM has been successfully tested for the separation of the lanthanide elements from monazite mineral, and seems a promising green nanotechnology, particularly suitable for urban mining.

Keywords: lanthanide separation; magnetic nanohydrometallurgy; complexing nanoparticles; magnetic nanoparticles; magnetophoresis; monazite processing; urban mining

1. Introduction

As the major group of the rare earth (REE) elements, lanthanides are increasingly important in modern technology because of their remarkable performance in optical, electronic and magnetic materials [1]. They are relevant in catalysis [1], metallurgy, ceramics, medicine [2–5], electronics, and energy [6,7], being also widely used in domestic apparatus such as TV (Eu, Ce), computer monitors (Ce, Nd), cell phones (La, Y, Nd, Gd, Dy, Eu, Tb), fluorescent lamps (Ce, La, Eu, Y, Tb), as well as in solar panels (La), aircrafts, automobile parts (La, Ce, Y, Dy, Eu), and wind turbines (Nd, Dy) [7].

The most important lanthanide minerals are represented by monazite, bastnäsite and xenotime. Monazite is a phosphate mineral of REE, rich in light elements such as Ce (46%), La (23%), Nd (19%), Pr (5%), Sm (3%), and Gd (1.7%), with less than 1% of the remaining lanthanides, in addition to Th. Similarly, bastnäsite is a fluorocarbonate mineral containing the light elements Ce (50%), La (32%), Nd (13%), and Pr (4%). It should be noticed that such light elements are the most relevant ones in

modern technology, accounting for about 95% of global world consumption. In particular, Nd demand is becoming increasingly important, because of its use in commercial supermagnets based on $\text{Nd}_2\text{Fe}_{14}\text{B}$ alloys. Xenotime is an yttrium phosphate mineral encompassing the major heavy elements Dy (7%), Er (6.2%), Yb (6%), Gd (3.6%), Ho (2%), Tm (1.2%), Sm (1.2%), and Tb (1%).

China is currently the main world producer, possessing the largest known reserves (55 Mt). Recent discoveries are placing Brazil in the second world position [7,8], with confirmed reserves of 22 Mt. Although Brazil has pioneered the rare earth production in the mid-20th century, such competence has been lost and the country is no longer a REE producer [9].

Lanthanide processing involves the crushing of the ore into a gravel size, followed by milling, and flotation. The collected materials are then treated with acids or alkalis. In this process, the existing thorium and cerium elements are removed as thorium phosphate and CeO_2 products, leaving aqueous concentrates of dissolved light lanthanide elements. Such concentrates are then chemically treated to undergo solvent extraction and ionic exchange processes [10–16]. However, since the lanthanide elements are chemically very similar, their separation becomes rather difficult. The complexation equilibrium constants involved span only a narrow range, where the minor differences are dictated by trends in the so-called lanthanide contraction series accompanying the increase of the atomic number.

In the last years, we have been working on a new nanotechnological approach to hydrometallurgy, based on iron oxide nanoparticles functionalized with suitable complexing agents for capturing and processing the metal ions in solution. It has been denominated magnetic nanohydrometallurgy (MNHM) [17–21] and can be performed under mild conditions in aqueous solution, similarly to conventional hydrometallurgy. The difference, however, is that after sequestering the metal ions, the complexing superparamagnetic nanoparticles can be magnetically confined and isolated, allowing to selectively extract and collect the elements according to their stability constants. In the case of transition metal elements, the nanoparticles have been collected directly onto the electrode surfaces, using external magnets, allowing to perform electrowinning and obtaining the pure elements. After electrodeposition, the active nanoparticles are released just by removing the magnet, returning to the process in a green and sustainable fashion. MNHM has already been successfully tested for copper(II), silver(I) and mercury(II) ions [19]. The technology can be completely automated [18], using small reactors, and is particularly suitable for urban mining.

In the case of the lanthanides, after their selective sequestering by the complexing nanoparticles, the elements can be released in acidic media, e.g., below pH 2, generating a solution enriched in the heavy elements. By adjusting the pH to 6, a new equilibrium takes place, increasing even more the amount of heavy elements on the complexing nanoparticles, according to their respective affinity constants. In this way, by using MNHM, lanthanide separation can be feasible, involving sequential complexation, confinement and releasing cycles. It can be carried out in aqueous solution and at room temperature, without using organic solvents, ionic exchange resins and exhaustive chemical processing.

2. Complexing Magnetic Iron Oxide Nanoparticles

Nanoparticles design is the key point in magnetic nanohydrometallurgy. In order to be employed as a magnetic carrier, one should use a suitable core material of nanometric size, exhibiting a large response to magnetic fields, in a superparamagnetic behavior. One of the best materials for this purpose is magnetite, Fe_3O_4 . It is widespread in nature and represents an environmentally compatible material. The black solid exhibits a mixed valence composition $\text{Fe}^{\text{II}}\text{Fe}^{\text{III}}_2\text{O}_4$ displaying the iron(II) ions in octahedral sites and the iron(III) ions equally distributed in octahedral and tetrahedral sites [22]. The nanoparticles exhibit nanocrystalline structure as shown in Figure 1. In the crystals, only the iron(II) ions contribute to the magnetization behavior of magnetite, since the iron(III) ions are antiferromagnetically coupled.

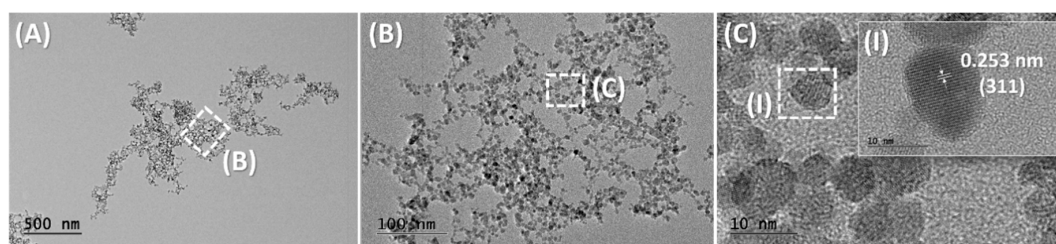


Figure 1. Transmission electron microscopy (TEM) images of nanocrystalline magnetite nanoparticles, in different magnifications (A–C). (I) Inset: Overfocused high resolution transmission electron microscopy (HRTEM) image of magnetite nanoparticle highlighting the interplanar distance of 311 plane (Scale bar: 10 nm).

The nanometric crystals exhibit typical magnetization values around $55\text{--}65 \text{ emu g}^{-1}$ at room temperature with little hysteresis ($H_c < 13 \text{ Oe}$), reflecting the existence of single magnetic domains. Magnetite is a stable material that can be easily prepared in large amounts, with low cost, by several methods, including the controlled oxidation of iron(II) polymeric complex suspensions [23], coprecipitation of iron(II) and iron(III) hydroxides [24], and the thermal decomposition of iron(III) metal organic complexes in organic media [25]. A similar alternative is maghemite, $\gamma\text{-Fe}_2\text{O}_3$, a brown solid composed exclusively by iron(III) ions. It can be obtained by the air oxidation under stirring and reflux for 3 h, of magnetite suspensions [26]. Its typical saturation magnetization, around $40\text{--}50 \text{ emu g}^{-1}$, is slightly smaller in relation to magnetite, but it exhibits greater stability in air. For this reason, most magnetite suspensions are slowly converted into the maghemite form after ageing under normal conditions.

Both magnetite and maghemite exhibit a superparamagnetic behavior characterized by the lack of hysteresis, or magnetic memory. This behavior can be seen in their corresponding magnetization plots, by scanning the magnetic field in a cyclic way, leading to superimposed curves in the two directions, as shown in Figure 2. The lack of hysteresis implies the existence of very weak interconversion barriers between the spin states, leading to a single magnetic domain. At very low temperatures, a very small hysteresis is often observed, reflecting the particularities of the nanoparticle structures. The superparamagnetic behavior is particularly relevant for magnetic nanohydrometallurgical applications, because it allows to readily disperse the nanoparticles after the capture and release of the metal ions, just by removing the magnetic [27]. In this way, the nanoparticles can be reused in a new cycle, without forming permanent agglomerates.

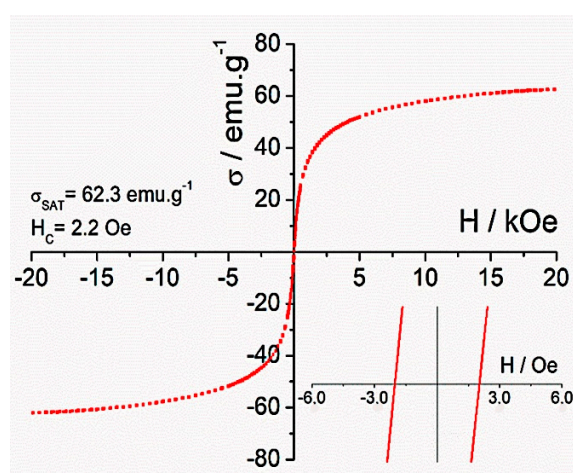
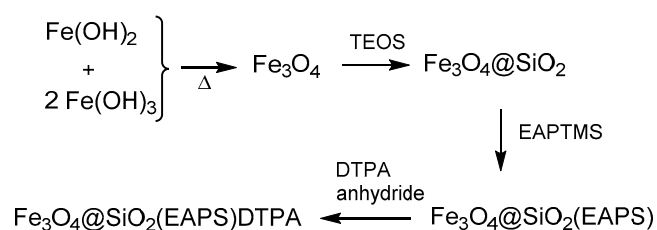


Figure 2. Magnetization curve for $\text{Fe}_3\text{O}_4@\text{SiO}_2$ nanoparticles, at room temperature, showing a negligible hysteresis effect ($H_c = 2.2 \text{ Oe}$) in the expanded scale (inset).

In order to extend their lifetime and protect from the chemical environment, the nanoparticles can be coated with a thin silicate layer, by treating with tetraethoxysilane (TEOS) according to the Stöber method [28]. This step can be followed by the treatment with ethylenediaminopropyltrimethoxysilane (EAPTMS) in order to introduce the chemical linkers required for binding the DTPA complexing agent via the amino/anhydride reaction. The overall procedure is shown in Scheme 1.



Scheme 1. Synthetic routes for obtaining the complexing nanoparticles.

The coating of the magnetic core with silica helps in preventing the exposure of the surface metal ions, thus precluding the interaction with the solvent and electrolytes, including the lanthanide ions and buffers. The silica coating also improves the protection against air, decreasing the conversion rates of magnetite into maghemite, and preventing the decay of the magnetization properties. In addition, the protecting coating is also important for anchoring aminoalkylsilane linkers, such as ethylenediaminepropyltrimethoxysilane, EAPTMS, required for attaching the final complexing agents. In the case of the lanthanide ions, because of their hard-base characteristics, the diethylenetriaminepentaacetic acid (DTPA) ligand is one of the best choices as a sequestering agent. This complexing agent can be covalently linked to the anchored (ethylenediamine)propylsilane (EAPS) group, via the reaction with DTPA anhydride, through the formation of amide bonds, as shown in Figure 3. The final, engineered nanoparticles $\text{Fe}_3\text{O}_4@\text{SiO}_2/\text{EAPS}/\text{DTPA}$ will be simply referred to as NP@DTPA, except when their specific composition becomes relevant.

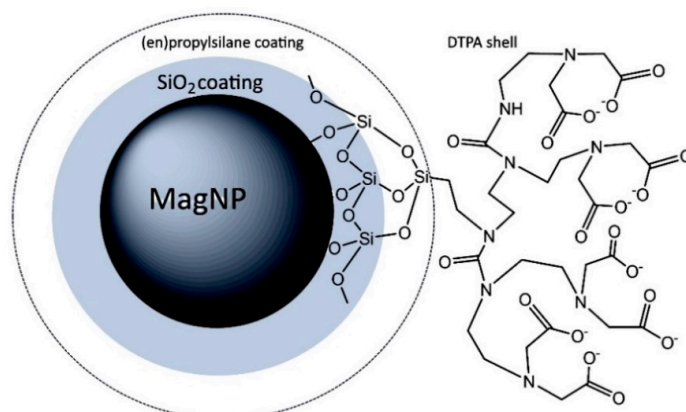


Figure 3. Magnetic nanoparticles protected by a SiO_2 coating, containing an (ethylenediamine)propylsilane shell for supporting the covalently bound DTPA molecules, $\text{Fe}_3\text{O}_4@\text{SiO}_2/\text{EAPS}/\text{DTPA}$, or simply NP@DTPA (adapted with permission from [29]).

The stepwise functionalization monitored by means of elemental analysis leads to a systematic increase of C and N content, accompanying the binding of the organosilane and DTPA agents, in the $\text{Fe}_3\text{O}_4@\text{SiO}_2/\text{EAPS}$ and $\text{Fe}_3\text{O}_4@\text{SiO}_2/\text{EAPS}/\text{DTPA}$ nanoparticles. The presence of the organic coating can also be seen in the FTIR spectra, as illustrated in Figure 4.

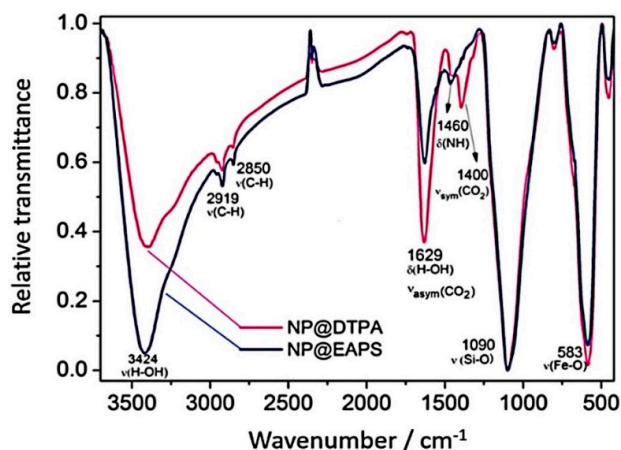


Figure 4. Typical FTIR spectra of the (—) $\text{Fe}_3\text{O}_4@SiO_2/EAPS$ and (—) $\text{Fe}_3\text{O}_4@SiO_2/EAPS/DTPA$ nanoparticles (adapted with permission from [29]).

The vibrational spectra of these two particles exhibit characteristic broad peaks at 1460 cm^{-1} ascribed to $\nu(N-H)$ stretching, and the sharp peaks at 2850 and 2919 cm^{-1} ascribed to $\nu(C-H)$ vibrations. Strong peaks observed at 1090 cm^{-1} correspond to $\nu(Si-O-Si)$ vibrations, while the $\nu(Fe-O)$ peaks are shown at 583 cm^{-1} , in agreement with the magnetite composition. Differential peaks can be observed in the $1600\text{--}1400\text{ cm}^{-1}$ region, corresponding to the asymmetric and symmetric stretching vibrations of the carboxylate groups. The peak at 1630 cm^{-1} corresponds to the $\nu_{asym}(CO_2)$ vibration, but it seems superimposed to the $\delta(O-H)$ vibrations of the water molecules present in the system. The relative intensity peak is stronger for the DTPA particles, as expected for the presence of the large number of carboxylate groups in relation to $\text{Fe}_3\text{O}_4@SiO_2/EAPS$. The weak peak at 1465 cm^{-1} is associated with $\nu(N-H)$ vibrations in both cases, but there is a differential peak at 1400 cm^{-1} for the $\text{Fe}_3\text{O}_4@SiO_2/EAPS/DTPA$ particle, corresponding to the $\nu_{sym}(CO_2)$ vibration. The $\text{Fe}_3\text{O}_4@SiO_2/EAPS$ and $\text{Fe}_3\text{O}_4@SiO_2/EAPS/DTPA$ nanoparticles were also monitored by dynamic light scattering and zeta potential measurements, as shown in Figure 5.

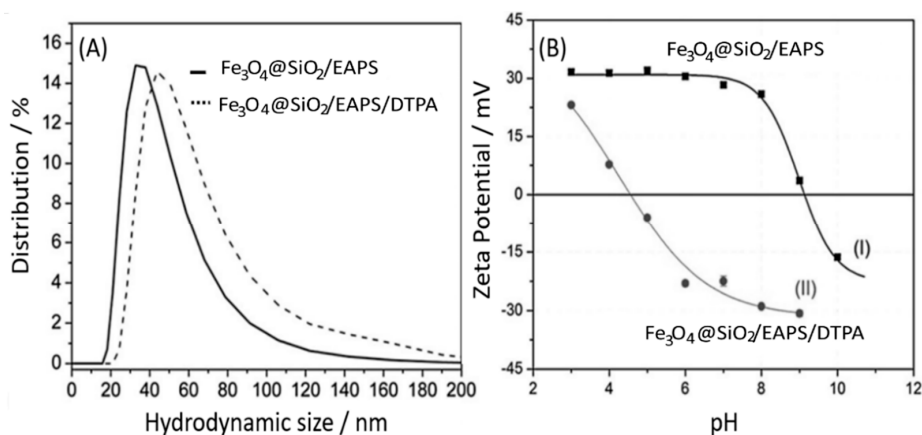


Figure 5. (A) Hydrodynamic sizes of the $\text{Fe}_3\text{O}_4@SiO_2/EAPS$ and of the $\text{Fe}_3\text{O}_4@SiO_2/EAPS/DTPA$ nanoparticles and (B) variation of their corresponding zeta potentials as a function of pH (adapted with permission from [29]).

In Figure 5A, the comparison between $\text{Fe}_3\text{O}_4@SiO_2/EAPS$ and the $\text{Fe}_3\text{O}_4@SiO_2/EAPS/DTPA$ nanoparticles shows that the external DTPA shell increases slightly the nanoparticles hydrodynamic size, as expected theoretically. Its presence is also reflected in the nanoparticles' zeta potentials, as shown in Figure 5B. The zeta potentials refer to electrokinetic potentials measured at the interfacial double layer also denoted as a slipping plane relative to the bulk fluid away from the interface [30]. It

is particularly related to the surface plane where the nanoparticles interact with the metal ions ion solution. In addition, the zeta potentials are important for promoting the nanoparticles stability in solution by means of electrostatic repulsion forces [31].

As shown in Figure 5B, the $\text{Fe}_3\text{O}_4@\text{SiO}_2/\text{EAPS}$ nanoparticles containing ethylenediamine groups are protonated below pH 8, leading to positive zeta potentials around 30 mV. Such high positive charges stabilize the nanoparticles in solution. The isoelectric point is observed at pH 9.12, where the electrostatic stability is lost. In the case of the $\text{Fe}_3\text{O}_4@\text{SiO}_2/\text{EAPS}/\text{DTPA}$ nanoparticles, the zeta potentials at low pH are a little smaller, starting at 20 mV at pH 3, indicating a positive charge from the protonation of the amino groups, in the presence of the neutral carboxylic acid groups. The isoelectric point occurs at pH 4.4, where the partial deprotonation of the carboxylic groups compensates the positive charges of the protonated amino groups. Above pH 5 most carboxylic groups are deprotonated, and the nanoparticles become electrostatically stabilized by a negative charge, corresponding to -30 mV potential.

3. Lanthanide Capture by the Iron Oxide Nanoparticles

DTPA is a well-known complexing agent for metal ions, and perhaps the best one in the market, for lanthanide ions. Its interaction with metal ions in aqueous solution can be readily probed by separating the superparamagnetic nanoparticles using an external magnet and analyzing its metal content, as well as of the remaining solution, by means of chemical, spectroscopic or X-ray fluorescence techniques.

For a systematic work, it is important to find the best experimental conditions, considering the pKa and the zeta potentials involved, using controlled conditions and the same batch of iron oxide nanoparticles in order to keep constant the chemical and physical parameters, such as composition, size, mobility, and complexation activity. This is a very important precaution, because the nanoparticle characteristics depend upon the synthetic procedures employed, turning the direct comparison with related nanoparticles obtained from different batches or methods, which is not always feasible. For comparison purposes, only a few related systems have been reported in the literature since our first work on MNHM in 2011 [21], or on the lanthanum/neodymium separation in 2016 [32]. In particular, one should mention those based on metallic iron [33], or using polymeric coating [34], which, in spite of their different scopes and methodologies, there is a good agreement with the lanthanide sequestering properties reported in our work.

It should be noted that the experiments involving the capture of lanthanide ions by the NP@DTPA nanoparticles have been carried out at pH 6 [32]. At this pH, most of the carboxylic groups are in the anionic form, and the nanoparticles are stabilized by the electrostatic repulsion from the surface carboxylate charges, as described by the DLVO theory [35]. In addition, at this pH, there is no risk of precipitating the lanthanide hydroxides before performing the complexation reaction. Another point observation is that for technological applications, MNHM requires suitably engineered iron oxide nanoparticles, exhibiting, for instance: (i) strong magnetic cores, with crystalline structures, displaying little hysteresis at room temperature; (ii) great stability in aqueous solution, in order to perform under normal conditions, e.g., in the presence of oxygen (air), high stirring rates and variable pH; (iii) large surface area and great mobility in solution; (iv) a protecting coating for preserving the magnetic core from the chemical environment; (v) a functional external coating encompassing the complexing agents; (vi) a large concentration of the complexing agents at the surface, in order to improve the yield of sequestered metal ions; (vii) a good chemical reversibility for exchanging the complexed metal ions with protons in the processing steps and performing the separation process; (viii) high magnetic recovery rates for effectively recycling the functional nanoparticles; (ix) low toxicity and safe manipulation, offering minor risks for the environment; (x) low cost and allowing production in large scale for industrial applications.

In the complexation studies, it is important to start from stable nanoparticles in solution because of their mobility, thus improving the interaction of the DTPA groups with the metal ions in order to form strong chelate complexes. The analysis is facilitated by the easy removal of the nanoparticles,

magnetically, in order to perform energy dispersive X-ray fluorescence (EDXRF) measurements and evaluate the amount of captured metal ions [29]. Typical EDXRF data for Fe₃O₄@SiO₂/EAPS/DTPA nanoparticles containing Nd³⁺ ions, separately, and their residual content in solution, as well as of the bare Fe₃O₄ nanoparticles, are shown in Figure 6.

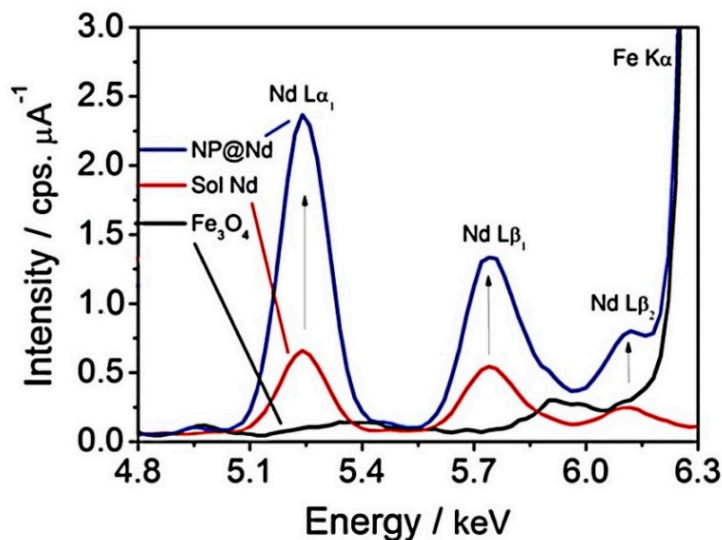
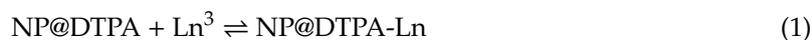


Figure 6. Typical X-ray fluorescence spectra of the Fe₃O₄ nanoparticles, of the neodymium nitrate solutions at 25 mmol L⁻¹, and of the nanoparticles after the capturing of Nd³⁺ ions (adapted with permission from [29]).

The complexation studies have been carried out for the several lanthanide ions, independently, in order to estimate their affinity or equilibrium constants. The process involves mobile nanoparticles and free ions in solution and can be described in terms of the Langmuir isotherms proposed for adsorption of molecules onto surfaces displaying similar binding sites, according to a monolayer distribution. There are also many other models available, such as the Freundlich isotherms, which can accommodate more complicated systems, including the formation of adsorption multilayers. In our case, the Langmuir isotherms have been preferred because their theoretical formalism keeps a close similarity with the chemical equilibrium in solution.

Considering the complexation equilibrium for the lanthanide ions (Ln³⁺) and the superparamagnetic nanoparticles, one can write:



where the equilibrium constant can be expressed by

$$K = \frac{[NP@DTPA - Ln]}{[Fe^{3+}][NP@DTPA]} \tag{2}$$

If θ is the fraction of the adsorption sites to which the Ln³⁺ ion has become attached, the fraction of the unattached sites is (1 - θ). Therefore,

$$\frac{[NP@DTPA - Ln]}{[NP@DTPA]} = \frac{\theta}{(1 - \theta)} \tag{3}$$

Calling the concentration of the lanthanide ions at equilibrium [Ln³⁺] = C_{eq} the adsorption constant can be written as

$$K = \frac{\theta}{C_{eq}(1 - \theta)} \tag{4}$$

or rearranging,

$$\theta = \frac{KC_{eq}}{(1 + KC_{eq})} \quad (5)$$

The adsorbed mass of lanthanide ions at equilibrium concentration is equal to the difference of the initial and equilibrium Ln^{3+} concentrations, C_o and C_{eq} , respectively. Defining q_{eq} as the adsorbed mass of lanthanide ions at equilibrium concentration per mass of adsorbent (m), NP, in a given volume V ,

$$q_{eq} = \frac{(C_o - C_{eq})V}{m} \quad (6)$$

Considering that

$$\theta = \frac{q_{eq}}{q_{max}} \quad (7)$$

it follows that

$$q_{eq} = \frac{KC_{eq}q_{max}}{(1 + KC_{eq})} \quad (8)$$

Therefore, the plot of q_e versus C_{eq} should exhibit a characteristic curvature, approaching a saturation point at higher concentrations of the lanthanides, corresponding to q_{max} . The corresponding plots for La^{3+} and Nd^{3+} ions can be seen in Figure 7.

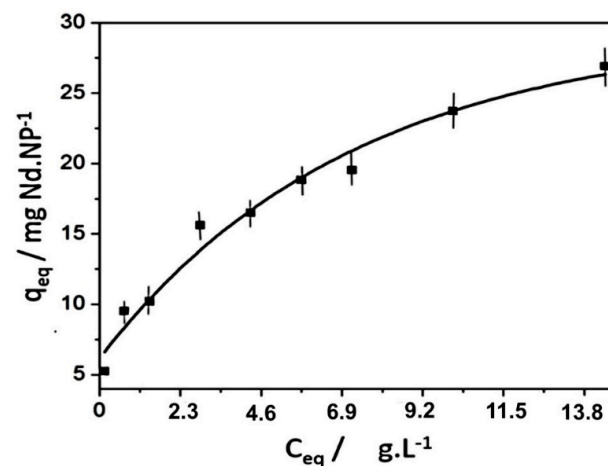


Figure 7. Adsorption isotherm of NP@DTPA in Nd^{3+} solutions at 298 K (adapted with permission from [29]).

A more convenient way is to express Equation (8) in the linearized form as shown in Figure 8.

$$\frac{C_{eq}}{q_{eq}} = \frac{1}{K q_{max}} + \frac{C_{eq}}{q_{max}} \quad (9)$$

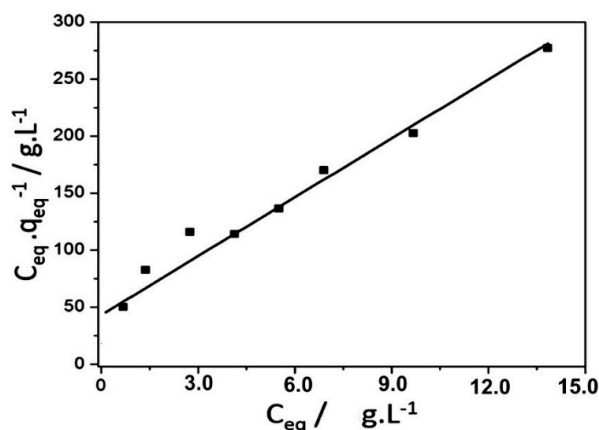


Figure 8. Linear plot of the adsorption isotherm of NP@DTPA in Nd^{3+} solutions based on the Langmuir Equation (9).

In this way, from the analysis of the linear data in Figure 8, the maximum coverage for the Nd^{3+} ions was evaluated as $28 \text{ mg}(\text{Nd}) \text{ g}(\text{NP})^{-1}$ and the equilibrium constant as $4.22 \times 10^{-4} \text{ g}(\text{NP}) \text{ L}^{-1}$.

4. Desorption Equilibrium

Desorption of the sequestered lanthanide ions in the NP@DTPA-Ln nanoparticles can be carried out by lowering the pH below 2 in order to protonate the carboxylate groups (Equation (10)).



The process can be monitored by X-ray fluorescence as illustrated in Figure 9. In this example, the NP@DTPA-Nd nanoparticles were magnetically confined, and the Nd content determined. After this, the particles were treated with an acidic solution, keeping the pH around 2. Then, after equilibration, the Nd content of the magnetic nanoparticle was analyzed again. As one can see, there is a complete release of the Nd^{3+} ions to the solution.

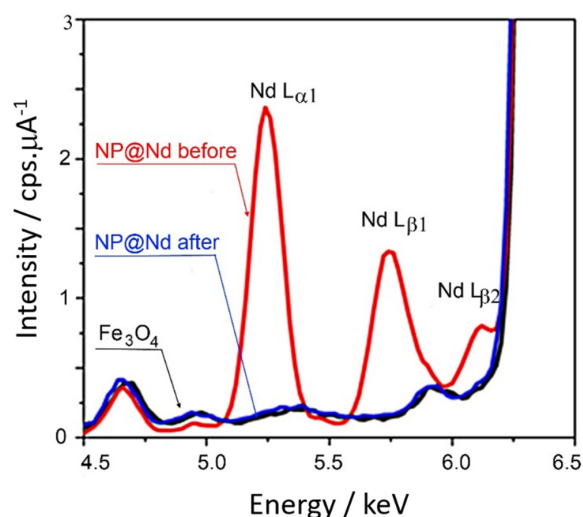


Figure 9. X-ray fluorescence analysis of the magnetic nanoparticles containing lanthanide ions, and after the treatment in acidic solutions at pH 2, showing the complete release of the metal elements (adapted with permission from [29]).

The reversible process can be controlled by the pH, allowing the use of the superparamagnetic nanoparticles in the separation of the lanthanide elements.

5. Magnetic Behavior, Kinetics and Magnetophoresis

Dy³⁺ ions have been specially employed for investigating the magnetic behavior, kinetics and magnetophoresis of the iron oxide nanoparticles because of their large magnetic moment. In addition, dysprosium is the major lanthanide component of the xenotime ore, being strategic in the fabrication of especially strong neodymium supermagnets. The capture of Dy³⁺ ions by the NP@DTPA nanoparticles can be represented as:



The process has been probed by the X-ray fluorescence spectra, by monitoring the corresponding L β_2 band, as shown in Figure 10.

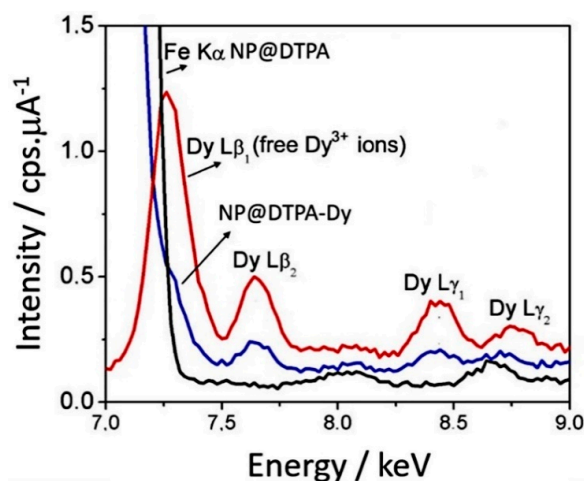


Figure 10. X-ray fluorescence spectra of the NP@DTPA, Dy³⁺ free ions in equilibrium, and NP@DTPA-Dy, after the magnetic confinement (adapted with permission from [35]).

The Langmuir isotherms were elaborated by determining the concentration of the remaining Dy³⁺ ions in solution, after confining the NP@DTPA-Dy particles with an external magnet. From the equilibrium concentrations of the Dy³⁺ ions, C_{eq} , the Langmuir isotherm was elaborated, as shown in Figure 11.

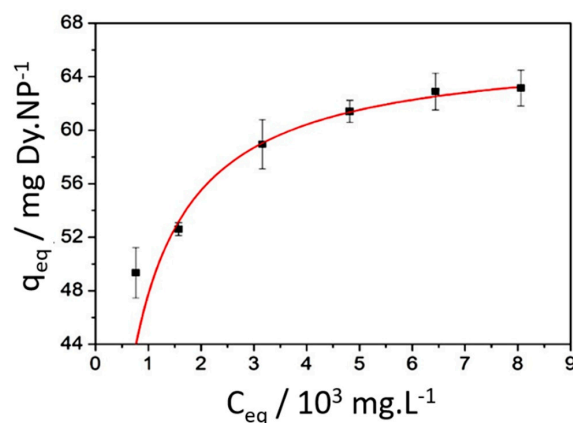


Figure 11. Adsorption isotherm of NP@DTPA in Dy³⁺ solutions at 298 K, pH 6, from the data collected after 500 min, under stirring, for ensuring complete equilibration (adapted with permission from [35]).

Its linearized form is shown in Figure 12.

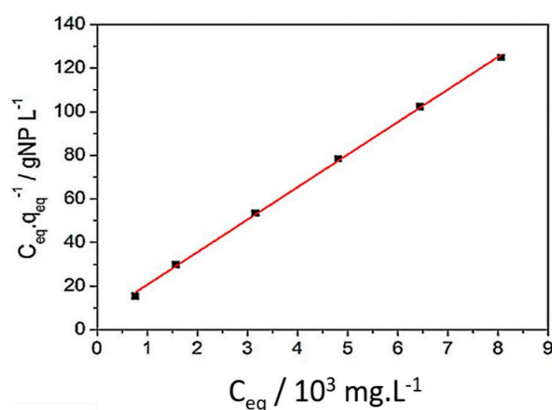


Figure 12. Linear plot of the adsorption isotherm of NP@DTPA in Dy^{3+} solutions, as expressed by the Langmuir equation.

In this way, the maximum coverage for the Dy^{3+} ions were $63.2 \text{ mg(Dy)/g(NP)}$, and the respective adsorption equilibrium constant was $2.57 \times 10^{-3} \text{ g(NP) L}^{-1}$. This value is significantly higher than the equilibrium constant of $4.22 \times 10^{-4} \text{ g(NP) L}^{-1}$, previously reported for the capture of Nd^{3+} ions, respectively, using the same superparamagnetic nanoparticles and experimental conditions. The formation of the surface metal complexes from the lanthanide capture has also been probed by scanning transmission electronic microscopy (STEM) using a high-angle annular dark field arrangement (HAADF) and shown in Figure 13 for the Dy^{3+} complex.

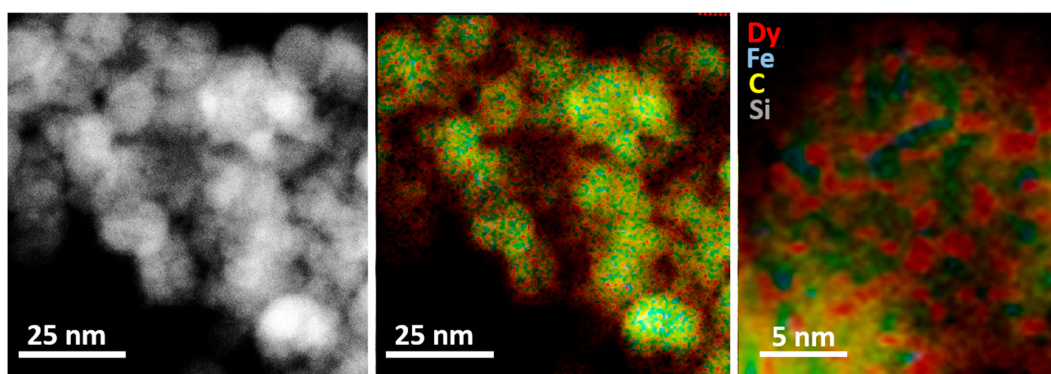


Figure 13. (Left) HAADF image of a cluster of NP@DTPA-Dy nanoparticles; (Middle) Elemental map image obtained by EDS analyses of the same NP@DTPA-Dy nanoparticles cluster. (Right) Enlarged image of the selected area from the middle image. The red, blue, yellow and green colors correspond to the presence of Dy, Fe, C and Si in the nanoparticles, respectively (adapted with permission from [35]).

In Figure 13, one can see the HAADF of the magnetic nanoparticles deposited on the carbon grid. The corresponding elemental map is also shown, revealing the distribution of the Dy (red), Fe (blue), C (yellow), and Si (green) elements at the NP@DTPA-Dy surface. In the more detailed image, one can see the red spots from the dysprosium ions located over the yellow stain of the carbon atoms from the DTPA ligand. As a matter of fact, this image represents the direct observation of the Dy-DTPA complexes at the nanoparticles surface. The surface metal complexes can influence the magnetism of the NP@DTPA-M nanoparticles by changing their electronic content at the surface. Their effect is expected to be more intense in the case of strongly paramagnetic metals, such as the Dy^{3+} ($4f^9$) species, where the intrinsic paramagnetism can couple with the magnetic field of the core. In this case, the magnetization of NP@DTPA-Dy nanoparticles (8.5 mg) containing 6.3% (weight) Dy^{3+} ions were recorded in water/glycerol suspension, using a vibrating sample (VSM) magnetometer. The measurements were carried out in comparison with the NP@DTPA (8.4 mg) sample with no Dy^{3+} ions.

The results are shown in Figure 14. Surprisingly, the binding of paramagnetic Dy^{3+} ions seems to decrease saturation magnetization of the NP@DTPA-Dy nanoparticles, as shown in Figure 14.

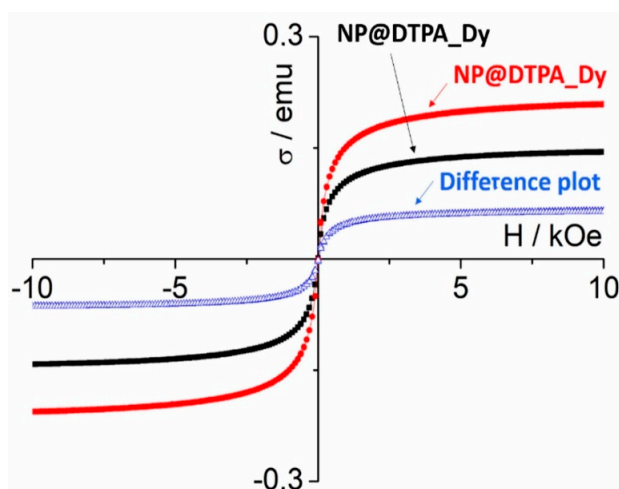


Figure 14. VSM measurements, at room temperature of NP@DTPA and NP@DTPA-Dy suspensions in water/glycerol mixture, showing the decrease of the magnetization promoted by the Dy^{3+} ions, as evaluated by the difference plot (adapted with permission from [35]).

In principle, the paramagnetic lanthanide ions were expected to enhance the saturation magnetization of the nanoparticles. However, the measurements indicated an opposite behavior, raising questions about the occurrence of dipolar interactions with the magnetic core. The HAADF image seems to corroborate the model illustrated in Figure 15, where Dy^{3+} ions are under the influence of opposing magnetic lines of the Fe_3O_4 core, leading to antiferromagnetic dipolar interactions.

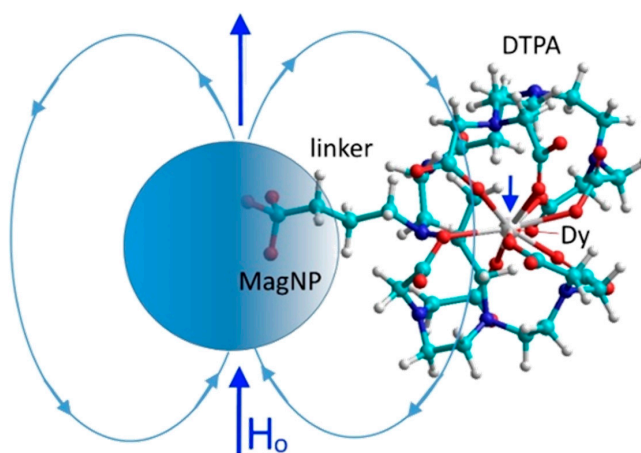


Figure 15. A pictorial representation of the antiferromagnetic dipolar interaction between dysprosium ions and the magnetic nanoparticles (adapted with permission from [35]).

Another way of probing the magnetic behavior of the particles is by monitoring their migration under the influence of an applied magnetic field. This response is known as magnetophoresis and is currently being investigated by many authors, using different techniques. Its understanding is essential for the application of nanoparticles in magnetic separation processes [35–42]. Since magnetic nanoparticles are very small, their magnetophoretic pathway can be perturbed by the thermal energy and the viscous drag forces [42]. For this reason, a strong magnetic force is necessary to overcome the thermal randomization. Because of the high complexity of the analytical solutions dealing with migration in inhomogeneous magnetic fields, the rigorous theoretical formalisms become rather complicated and are beyond the scope of this paper. As a simple approximation, the magnetophoretic

velocity v , can be obtained by equilibrating the force involved in the magnetophoretic displacement of the isolated nanoparticles of radius R and magnetic moment m , under a magnetic field H , and gradient $(\partial H/\partial r)$, and the opposing viscous drag force, as

$$v = \frac{1}{6\pi\eta R} \chi\mu_0 H \frac{\partial H}{\partial r} \quad (12)$$

where μ_0 is the magnetic constant (equal 1 in cgs unit), and η is the viscosity.

In this way, the magnetophoretic velocity of the nanoparticles should be directly proportional to the magnetic field and to the magnetic field gradient, as well as to the magnetic moment or susceptibility of the particles, and inversely proportional to their hydrodynamic sizes. A simple arrangement for probing magnetophoresis in the laboratory is by using an analytical balance equipped with a suitable cantilever for allowing external weighing, as shown in Figure 16. The sample probe employed is just a miniature tube, placed above of small $\text{Nd}_2\text{Fe}_{14}\text{B}$ supermagnet (diameter = 1 inch) at a constant distance and position, in order to provide the same magnetic field and gradients. A pictorial representation of the experiment is shown in Figure 17 [35].



Figure 16. (A–E) Monitoring the magnetophoresis of NP@DTPA in the presence of a $\text{Nd}_2\text{Fe}_{14}\text{B}$ magnet, as a function of time by means of an external weight device placed on the analytical balance pan (only the cantilever is shown) (adapted with permission from [43]).

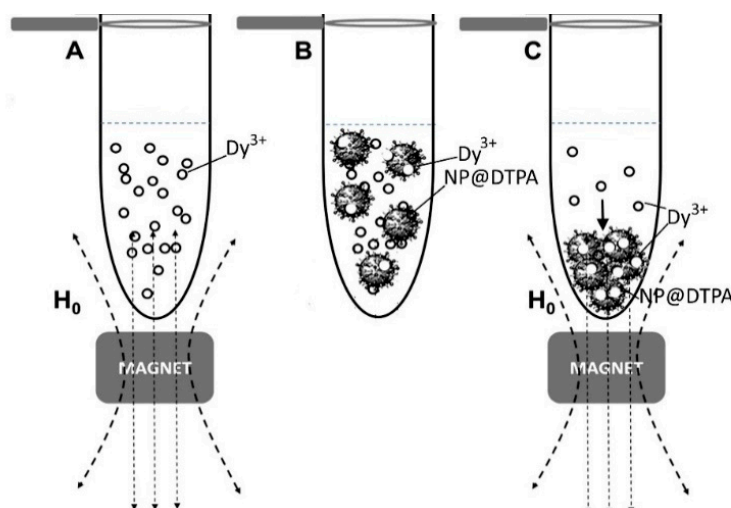


Figure 17. Pictorial representation of the capture of Dy^{3+} ions in the presence of the magnet: (A) Initial Dy^{3+} solution (0.1 mol L^{-1}); (B) after adding NP@DTPA and stirring without applying the magnet; (C) magnetophoretic deposition after the capture of Dy^{3+} ions by the superparamagnetic nanoparticles (adapted with permission from [43]).

By using this arrangement, it is possible to evaluate the average magnetophoretic rates by monitoring the relative weight increase as the magnetic nanoparticles reach the bottom attracted by the magnetic field. The presence of paramagnetic ions in solution has only a negligible effect on the weight increase by the attracted nanoparticles, since their magnetic moments differ by 8 orders of magnitude.

In a typical magnetophoretic experiment, by starting with 1 mL of $0.1 \text{ mol L}^{-1} \text{ Dy}^{3+}$ solution, 8 mg of NP@DTPA was added and the mixture was kept under stirring for 5 h to ensure equilibration. After this, the sample was kept in the external weighing device, and a magnetic field was applied to promote the nanoparticles deposition at the bottom, while measuring the weigh increase as a function of time. A similar experiment was repeated in the absence of Dy^{3+} ions. The comparison, shown in Figure 18, revealed that a systematic decrease of magnetism, by $5.9 \pm 1\%$ results after the binding of the Dy^{3+} ions.

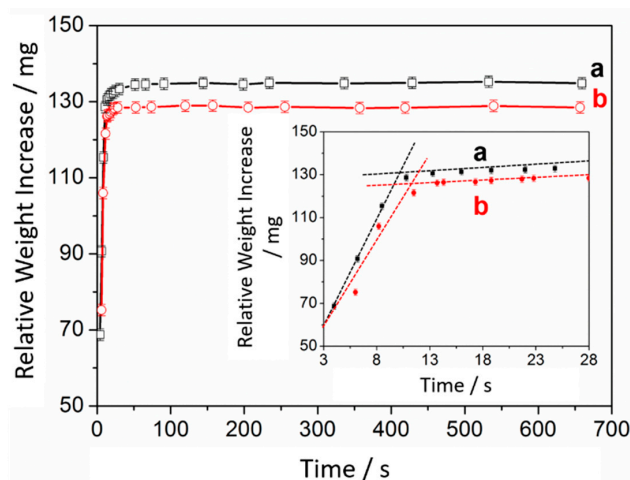


Figure 18. Magnetophoresis of NP@DTPA before (a) and after (b) the binding of Dy^{3+} ions (magnet distance = 0.40 cm) showing the decrease of magnetization in the presence of the lanthanide ions and the slower magnetophoretic rate (inset) (adapted with permission from [43]).

This result is consistent with the occurrence of an anti-ferromagnetic coupling between the paramagnetic Dy^{3+} ions and the superparamagnetic core, as already observed by VSM, Figures 14 and 15. The magnetophoretic velocity is also slightly reduced after the binding of Dy^{3+} ions, with the curve slopes decreasing from 8.98 to 8.52. This is consistent with the decrease of the magnetization of the nanoparticles and with the increase of the hydrodynamic radii due to the presence of the Dy^{3+} ions. The observed decrease of magnetization is correlated with the amount (6% w/w) of captured Dy^{3+} ions, allowing to probe the metal ion extraction, using a simple analytical balance.

6. Lanthanide Separation

The equilibrium constants for the complexation of the lanthanide ions have been obtained using the same batch of NP@DTPA nanoparticles, for which all the chemical and physical constants have been previously determined. They have been evaluated from the corresponding Langmuir isotherms, generated under the same conditions, at room temperature, for the La^{3+} , Pr^{3+} , Nd^{3+} , Sm^{3+} , Gd^{3+} and Dy^{3+} ions, leading to the following equilibrium constants: 2.9×10^{-4} , 4.0×10^{-4} , 4.2×10^{-4} , 6.7×10^{-4} , 1.2×10^{-3} , $2.3 \times 10^{-3} \text{ g(NP) L}^{-1}$, respectively. As shown in Figure 19, the trends in the equilibrium constants are dictated by the lanthanide contraction series, where a smaller ionic radius leads to the formation of a stronger complex.

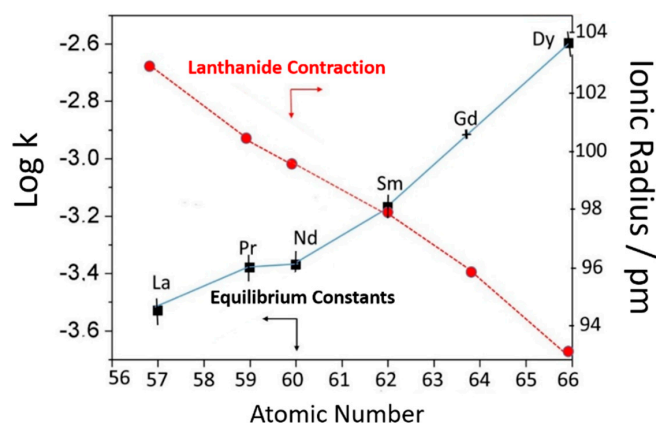


Figure 19. Affinity constants (K) of the lanthanide elements as a function of the atomic number, superimposed to the corresponding radial contraction plot (adapted with permission from [44]).

Lanthanide elements separation using NP@DTPA can be performed using the same classical chelation chemistry employed in hydrometallurgy for rare earths. For instance, using an ionic exchange resin column, the lanthanide ions are loaded at the top and gradually eluted with complexing agents under controlled pH. Complexation can remove the lanthanide ion from the column, but a rather complex equilibrium network takes place, requiring long columns and a very careful procedure. In magnetic nanohydrometallurgy, the lanthanide ions are selectively sequestered by the complexing nanoparticles, according to their specific affinity constants, and can be readily confined with a magnet. The confined nanoparticles are enriched by the heavy elements, considering the specific affinity trends shown in Figure 18. Then, in a second cycle, such confined nanoparticles are suspended in an aqueous solution maintained at pH 2 or less, in order to release the complexed metal ions by the protonation of the carboxylate groups as illustrated in Figure 20.

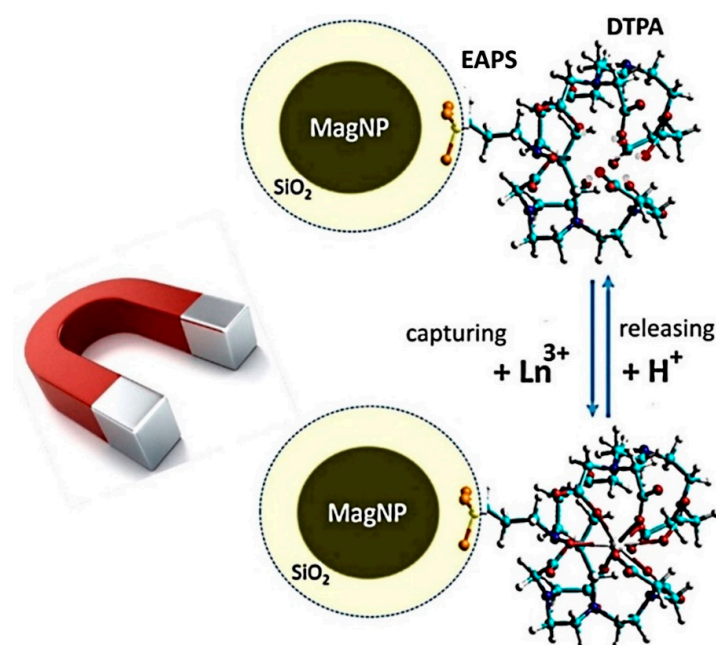


Figure 20. Magnetic capture and releasing of lanthanide ions by the superparamagnetic nanoparticles functionalized with DTPA (adapted with permission from [44]).

Then the pH is adjusted to 6 in order to restore the complexing capability of the particles, but now in the presence of the lanthanide ions in solution, enriched with heavy elements. Complexation

does enhance the heavy elements removal from the solution. The magnetic confinement and release cycle can be repeated again and again in order to sequentially separate the heavy lanthanides from the light ones. The chemistry resembles the classical extraction of lanthanides using complexing agents and solvents. However, it is much simpler, involving just a one pot procedure, without using solvents or columns.

6.1. Binary Mixtures

Lanthanide separation studies were initially applied to binary mixtures, such as Nd^{3+} and La^{3+} ions [31,33,43,44] as a proof of concept. The experiment started with an equimolar mixture of the two elements, and the first cycle of complexation with the complexing nanoparticles was performed. In this particular case, the analysis of the elements captured by the nanoparticles led to a distribution of 66% Nd^{3+} and 33% La^{3+} . This result is in perfect agreement with their corresponding affinity constants. In a second step, after confining the nanoparticles with a magnet, a subsequent treatment with diluted acids (pH 2) released the lanthanide ions into a new solution, keeping the 66:33 proportion. Then, the pH was raised up to 6, and a new complexation equilibrium took place. The relative amounts of the two elements captured by the nanoparticles were 94% Nd^{3+} and 6% La^{3+} . In the third step, starting from the 94:6 ratio, the amount of captured Nd^{3+} ions were >99%, since no evidence of La^{3+} could be detected by the X-ray fluorescence technique (Figure 21).

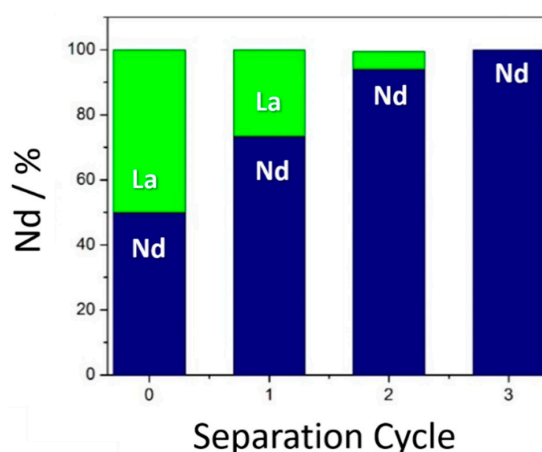


Figure 21. Fractionation of La^{3+} and Nd^{3+} mixtures, starting from an equimolar solution (stage 0) and subsequent MNHM processing by using superparamagnetic nanoparticles functionalized with DTPA, as described in the text (adapted with permission from [29]).

The enrichment plots illustrated in Figure 21 indicate that three partition steps can be enough to obtain Nd^{3+} in pure form, by starting from an equimolar mixture with La^{3+} ions. A similar test was applied for La^{3+} and Sm^{3+} , by starting with an equimolar mixture of the lanthanide. The distribution of the lanthanide ions in the first step was about 81% Sm^{3+} and 19% La^{3+} , reflecting the expected trends from the DTPA- Ln^{3+} stability constants. A subsequent treatment of the collected nanoparticles with diluted acid (pH 2) led to a complete release of the lanthanide ions. After this step, the second cycle was performed, now starting from the 81/19 ($\text{Sm}^{3+}/\text{La}^{3+}$) ratio. The analysis of the collected superparamagnetic nanoparticles from the second cycle revealed undetectable amounts of La^{3+} ions, using the X-ray fluorescence instrument. This result is illustrated in Figure 22. Binary mixtures of $\text{La}^{3+}/\text{Sm}^{3+}$ and $\text{La}^{3+}/\text{Gd}^{3+}$ ions have also been easily separated after two cycles.

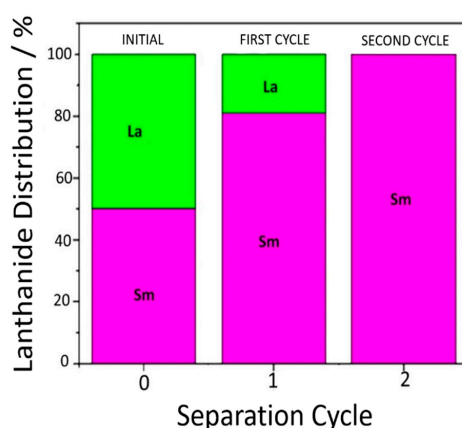


Figure 22. Fractionation of a binary mixture, starting from an equimolar solution (stage 0) of La^{3+} and Sm^{3+} ions, and treating with superparamagnetic nanoparticles functionalized with DTPA, as described in the text (adapted with permission from [44]).

6.2. Ternary Mixtures

Starting with a ternary mixture comprising equimolar amounts of La^{3+} , Nd^{3+} and Gd^{3+} ions (10 mL, 0.10 mol L^{-1}), 10 mg of NP@DTPA was added (pH 6) and kept under gently stirring at room temperature for 6 h. The starting proportion was 33:33:33 (%), respectively. After collecting the iron oxide nanoparticles, the following proportion 13:47:40 (%) of the three elements was obtained, respectively. After releasing the lanthanides at pH 2, the capture process was repeated for the same lanthanide proportion in solution, at pH 6.0. The analytical data collected after the second cycle revealed 75% Gd^{3+} over 25% Nd^{3+} , with no evidence of La^{3+} ions. In the third sequential cycle, the contents of Gd^{3+} ions were practically 100%, as illustrated in Figure 23.

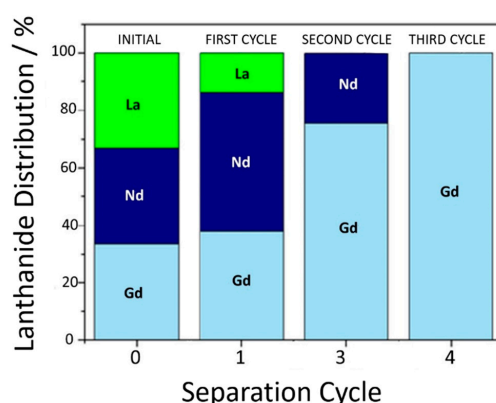


Figure 23. Fractionation of a ternary mixture, starting from equimolar amounts (stage 0) of Gd^{3+} , Nd^{3+} and La^{3+} ions, by using superparamagnetic nanoparticles functionalized with DTPA (adapted with permission from [44]).

6.3. Lanthanide Separation from Monazite

After performing the separations of binary and ternary mixtures, the MNHM process was applied to a lanthanide concentrate from monazite ore. The Ce and Th species present in the mineral were previously removed by precipitation, yielding a lanthanide concentrate containing approximately 45% La^{3+} , 36% Nd^{3+} , 9% Pr^{3+} , 6% Sm^{3+} , and 3% Gd^{3+} ions. The original sample was supplied by the Solvay Laboratory in Brazil, about 30 years ago, when our group was involved in a lanthanide separation project. Because of the ageing, this concentrate was also replicated in our laboratory, using analytical grade compounds. By starting from this mixture, at pH 6, the first cycle of capture exhibited a content of 36% Nd^{3+} , 6% Pr^{3+} , 30% Sm^{3+} , and 28% Gd^{3+} ions. In the second cycle, the following

distribution was obtained: 8% Nd³⁺, 50% Sm³⁺ and 42% Gd³⁺ ions. In the third cycle, only 46% Sm and 54% Gd³⁺ was observed. After the fourth cycle, the proportion became 26% Sm³⁺ and 74% Gd³⁺. In the fifth cycle, Gd³⁺ ions represented practically 100% of the sample as shown in Figure 24.

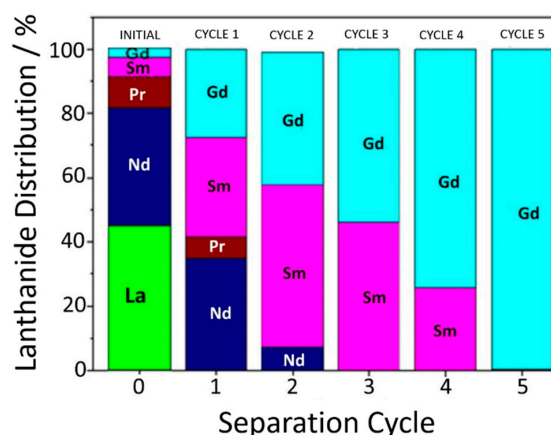


Figure 24. Sequential processing of a monazite concentrate by magnetic nanohydrometallurgy using NP@DTPA nanoparticles in aqueous solution (adapted with permission from [44]).

7. Conclusions

Magnetic nanohydrometallurgy employing iron oxide nanoparticles functionalized with ethylenediaminepropylsilane and the diethylenediaminepentaacetic acid agents can effectively capture lanthanide ions from aqueous solution, allowing their magnetic extraction at pH 6 and release below pH 2, respectively. Preferential binding of heavy lanthanides has been observed and is dictated by their affinity constants reflecting the lanthanide contraction series. For a binary mixture, a high separation efficiency (>99%) can be achieved after two or three successive complexation and release stages. As the number of components increases, more repetitive extraction cycles become necessary. Therefore, MNHM allows the separation of lanthanide elements using engineered nanoparticles, by performing under green and sustainable conditions, i.e., at room temperature, in aqueous solution, and mild pHs, dispensing the use of classical physical separation processes and organic solvents. It can be easily automated, allowing the use of small reactors. The technology can enable urban mining applications, for instance in the neodymium and dysprosium extraction from the magnet components of the electronic wastes.

Author Contributions: Methodology, investigation and writing, F.M.d.M.; conceptualization, investigation and methodology, S.N.A.; conceptualization, supervision and writing, H.E.T. All authors have read and agreed to the published version of the manuscript.

Funding: Fundação de Amparo à Pesquisa do Estado de São Paulo (FAPESP 2018/21489-1) and Conselho Nacional de Desenvolvimento Científico e Tecnológico (CNPq 405301/2013-8).

Acknowledgments: The authors are in debit to Alceu Totti Silveira for his help in X-ray fluorescence measurements and Ulisses Condomitti for this important contributions to the development of the MNHM technology.

Conflicts of Interest: The authors declare no conflict of interest.

References

- Edelmann, F. Lanthanides and actinides: Annual survey of their organometallic chemistry covering the year. *Coord. Chem. Rev.* **2009**, *253*, 2515–2587. [[CrossRef](#)]
- Wang, Q.; Nono, K.N.; Syrjanpaa, M.; Charbonniere, L.J.; Hovinen, J.; Harma, H. Stable and Highly Fluorescent Europium(III) Chelates for Time-Resolved Immunoassays. *Inorg. Chem.* **2013**, *52*, 8461–8466. [[CrossRef](#)] [[PubMed](#)]

3. Pihlasalo, S.; Kulmala, A.; Rozwandowicz-Jansen, A.; Hanninen, P.; Harma, H. Sensitive Luminometric Method for Protein Quantification in Bacterial Cell Lysate Based on Particle Adsorption and Dissociation of Chelated Europium. *Anal. Chem.* **2012**, *84*, 1386–1393. [[CrossRef](#)] [[PubMed](#)]
4. Teo, R.D.; Termini, J.; Gray, H.B. Lanthanides: Applications in Cancer Diagnosis and Therapy. *J. Med. Chem.* **2016**, *59*, 6012–6024. [[CrossRef](#)] [[PubMed](#)]
5. Shokrollahi, H. Contrast agents for MRI. *Mater. Sci. Eng. C. Mater. Biol. Appl.* **2013**, *33*, 4485–4497. [[CrossRef](#)] [[PubMed](#)]
6. Coey, J.M.D. Hard Magnetic Materials: A Perspective. *IEEE Trans. Magn.* **2011**, *47*, 4671–4681. [[CrossRef](#)]
7. Silva Junior, A.F.; de Campos, M.F. Relevance of Rare earth for the energy sector. *Holos* **2016**, *32*, 350–363.
8. Silva, G.A.; Petter, C.O.; Albuquerque, N.R. Factors and competitiveness analysis in rare earth mining, new methodology: Case study from Brazil. *Heliyon* **2018**, *4*, e00570. [[CrossRef](#)]
9. de Sousa Filho, P.C.; Galaco, A.R.B.S.; Serra, O.A. Rare Earths: Periodic table, discovery, exploration in Brazil and applications. *Quim. Nova* **2019**, *42*, 1208–1224.
10. De Jong, N.; Draye, M.; Favre-Réguillon, A.; LeBuzit, G.; Cote, G.; Foos, J. Lanthanum(III) and gadolinium(III) separation by cloud point extraction. *J. Colloid Interface Sci.* **2005**, *291*, 303–306. [[CrossRef](#)]
11. Hidayah, N.N.; Abidin, S.Z. The evolution of mineral processing in extraction of rare earth elements using solid-liquid extraction over liquid-liquid extraction: A review. *Miner. Eng.* **2017**, *112*, 103–113. [[CrossRef](#)]
12. Boubals, N.; Wagner, C.; Dumas, T.; Chaneac, L.; Manie, G.; Kaufholz, P.; Marie, C.; Panak, P.J.; Modolo, G.; Geist, A.; et al. Complexation of Actinide(III) and Lanthanide(III) with H(4)TPAEN for a Separation of Americium from Curium and Lanthanides. *Inorg. Chem.* **2017**, *56*, 7861–7869. [[CrossRef](#)] [[PubMed](#)]
13. Gras, M.; Papaiconomou, N.; Chainet, E.; Tedjar, F.; Billard, I. Separation of cerium(III) from lanthanum(III), neodymium(III) and praseodymium(III) by oxidation and liquid-liquid extraction using ionic liquids. *Sep. Purif. Technol.* **2017**, *178*, 169–177. [[CrossRef](#)]
14. Yamin, D.; Xiangguang, G.; Yanliang, W.; Zeyuan, Z.; Chao, H.; Xiaoqi, S. A separation processing for industrial rare earth feed solution by phosphonium ionic liquid type saponification strategy. *J. Rare Earths* **2017**, *35*, 290–299.
15. Sun, T.; Xu, C.; Chen, J.; Duan, W. Formation of W/O Microemulsions in the Extraction of the Lanthanide Series by Purified Cyanex 301. *Solvent Extr. Exch.* **2017**, *35*, 199–209. [[CrossRef](#)]
16. Larsson, K.; Cullen, T.D.; Mezyk, S.P.; McDowell, R.G.; Martin, L.R. Complications in complexation kinetics for lanthanides with DTPA using dye probe molecules in aqueous solution. *Rsc Adv.* **2017**, *7*, 26507–26512. [[CrossRef](#)]
17. Condomitti, U.; Zuin, A.; Novak, M.A.; Araki, K.; Toma, H.E. Magnetic coupled electrochemistry: Exploring the use of superparamagnetic nanoparticles for capturing, transporting and concentrating trace amounts of analytes. *Electrochem. Commun.* **2011**, *13*, 72–74. [[CrossRef](#)]
18. Condomitti, U.; Silveira, A.T.; Condomitti, G.W.; Toma, S.H.; Araki, K.; Toma, H.E. Silver recovery using electrochemically active magnetite coated carbon particles. *Hydrometallurgy* **2014**, *147–148*. [[CrossRef](#)]
19. Condomitti, U.; Almeida, S.N.; Silveira, A.T.; De Melo, F.M.; Toma, H.E. Green processing of strategic elements based on magnetic nanohydrometallurgy. *J. Braz. Chem. Soc.* **2018**, *29*, 948–959. [[CrossRef](#)]
20. Toma, H.E. Magnetic nanohydrometallurgy: A nanotechnological approach to elemental sustainability. *Green Chem.* **2015**, *17*, 2027–2041. [[CrossRef](#)]
21. Condomitti, U.; Zuin, A.; Silveira, A.T.; Araki, K.; Toma, H.E. Magnetic nanohydrometallurgy: A promising nanotechnological approach for metal production and recovery using functionalized superparamagnetic nanoparticles. *Hydrometallurgy* **2012**, *125*, 148–151. [[CrossRef](#)]
22. Mathew, D.S.; Juang, R.S. An overview of the structure and magnetism of spinel ferrite nanoparticles and their synthesis in microemulsions. *Chem. Eng. J.* **2007**, *129*, 51–65. [[CrossRef](#)]
23. da Silva, D.G.; Toma, S.H.; de Melo, F.M.; Carvalho, L.V.C.; Magalhaes, A.; Sabadini, E.; dos Santos, A.D.; Araki, K.; Toma, H.E. Direct synthesis of magnetite nanoparticles from iron(II) carboxymethylcellulose and their performance as NMR contrast agents. *J. Magn. Magn. Mater.* **2016**, *397*, 28–32. [[CrossRef](#)]
24. Yamaura, M.; Toma, H.E.; Camilo, R.L.; Sampaio, L.C.; Macedo, M.A.; Nakamura, M. Preparation and characterization of (3-aminopropyl) triethoxysilane-coated magnetite nanoparticles. *J. Magn. Magn. Mater.* **2004**, *279*, 210–217. [[CrossRef](#)]
25. Park, J.; An, K.; Hwang, Y.; Park, J.-G.; Noh, H.-J.; Kim, J.-Y.; Park, J.-H.; Hwang, N.-M.; Hyeon, T. Ultra-large-scale syntheses of monodisperse nanocrystals. *Nat. Mater.* **2004**, *3*, 891–895. [[CrossRef](#)] [[PubMed](#)]

26. de Melo, F.M.; Grasseschi, D.; Brandão, B.B.N.S.; Fu, Y.; Toma, H.E. Superparamagnetic Maghemite-Based CdTe Quantum Dots as Efficient Hybrid Nanoprobes for Water-Bath Magnetic Particle Inspection. *Acs Appl. Nano Mater.* **2018**, *1*, 2858–2868. [[CrossRef](#)]
27. Melo, F.M.; Silveira, A.T.; Quartaroli, L.F.; Kaid, F.F.; Cornejo, D.R.; Toma, H.E. Magnetic behavior of superparamagnetic nanoparticles containing chelated transition metal ions. *J. Magn. Magn. Mater.* **2019**, *487*, 165324. [[CrossRef](#)]
28. Stober, W.; Fink, A.; Bohn, E. Controlled grow of monodisperse silica spheresein micron size range. *J. Colloid Interface Sci.* **1968**, *26*, 62. [[CrossRef](#)]
29. Almeida, S.D.N.; Toma, H.E. Neodymium(III) and lanthanum(III) separation by magnetic nanohydrometallurgy using DTPA functionalized magnetite nanoparticles. *Hydrometallurgy* **2016**, *161*, 22–28. [[CrossRef](#)]
30. Bhattacharjee, S. DLS and zeta potential—What they are and what they are not? *J. Control. Release* **2016**, *235*, 337–351. [[CrossRef](#)]
31. Jesionowski, T.; Ciesielczyk, F.; Krysztafkiewicz, A. Influence of selected alkoxy silanes on dispersive properties and surface chemistry of spherical silica precipitated in emulsion media. *Mater. Chem. Phys.* **2010**, *119*, 65–74. [[CrossRef](#)]
32. Zhang, H.; McDowell, R.G.; Martin, L.R.; Qiang, Y. Selective Extraction of Heavy and Light Lanthanides from Aqueous Solution by Advanced Magnetic Nanosorbents. *Acs Appl. Mat. Interfaces* **2016**, *8*, 9523–9531. [[CrossRef](#)] [[PubMed](#)]
33. Cai, Y.; Yuan, F.; Wang, X.; Sun, Z.; Chen, Y.; Liu, Z.; Wang, X.; Yang, S.; Wang, S. Synthesis of core-shell structured Fe₃O₄@carboxymethyl cellulose magnetic composite for highly efficient removal of Eu(III). *Cellulose* **2017**, *24*, 175–190. [[CrossRef](#)]
34. Verwey, E.J.; Overbeek, J.T.G. *The Theory of the Stability of Lyophobic Colloids*; Dover: New York, NY, USA, 2000.
35. Melo, F.M.D.; Almeida, S.D.N.; Uezu, N.S.; Ramirez, C.A.O.; Santos, A.D.D.; Toma, H.E. Extraction of Dysprosium Ions with DTPA Functionalized Superparamagnetic Nanoparticles Probed by Energy Annular Dark Field Imaging. *J. Nanosci. Nanotechnol.* **2017**, *17*, 1–5.
36. Leong, S.S.; Ahmad, Z.; Lim, J. Magnetophoresis of superparamagnetic nanoparticles at low field gradient: Hydrodynamic effect. *Soft Matter* **2015**, *11*, 6968–6980. [[CrossRef](#)] [[PubMed](#)]
37. Benelmekki, M.; Martinez, L.M.; Andreu, J.S.; Camacho, J.; Faraudo, J. Magnetophoresis of colloidal particles in a dispersion of superparamagnetic nanoparticles: Theory and experiments. *Soft Matter* **2012**, *8*, 6039. [[CrossRef](#)]
38. Andreu, J.S.; Camacho, J.; Faraudo, J.; Benelmekki, M.; Rebollo, C.; Martínez, L.M. Simple analytical model for the magnetophoretic separation of superparamagnetic dispersions in a uniform magnetic gradient. *Phys. Rev. E-Stat. Nonlinearsoft Matter Phys.* **2011**, *84*, 1–8. [[CrossRef](#)]
39. Faraudo, J.; Andreu, J.S.; Camacho, J. Understanding diluted dispersions of superparamagnetic particles under strong magnetic fields: A review of concepts, theory and simulations. *Soft Matter* **2013**, *9*, 6654. [[CrossRef](#)]
40. Friedman, G.; Yellen, B. Magnetic separation, manipulation and assembly of solid phase in fluids. *Curr. Opin. Colloid Interface Sci.* **2005**, *10*, 158–166. [[CrossRef](#)]
41. Gómez-Pastora, J.; Bringas, E.; Ortiz, I. Recent progress and future challenges on the use of high performance magnetic nano-adsorbents in environmental applications. *Chem. Eng. J.* **2014**, *256*, 187–204. [[CrossRef](#)]
42. Lim, J.; Lanni, C.; Evarts, E.R.; Lanni, F.; Tilton, R.D.; Majetich, S.A. Magnetophoresis of nanoparticles. *Acs Nano* **2011**, *5*, 217–226. [[CrossRef](#)] [[PubMed](#)]
43. De Melo, F.M.; Almeida, S.D.N.; dos Santos, A.D.; Toma, H.E. Magnetophoresis of Superparamagnetic Nanoparticles Applied to the Extraction of Lanthanide Ions in the Presence of Magnetic Field. *Nanoworld J.* **2017**, *3*, 38–43. [[CrossRef](#)]
44. Almeida, S.D.N.; Toma, H.E. Lanthanide ion processing from monazite based on magnetic nanohydrometallurgy. *Hydrometallurgy* **2019**, *189*, 105138. [[CrossRef](#)]

